Article

InSAR Modeling and Deformation Prediction for Salt Solution Mining Using a Novel CT-PIM Function

Xuemin Xing [1,2,3], Tengfei Zhang [1,3], Lifu Chen [1,4,*], Zefa Yang [5], Xiangbin Liu [1,3], Wei Peng [1,3,5] and Zhihui Yuan [1,4]

1   Laboratory of Radar Remote Sensing Applications, Changsha University of Science & Technology, Changsha 410114, China; xuemin.xing@csust.edu.cn (X.X.); tengfei@stu.csust.edu.cn (T.Z.); liuxb0219@foxmaul.com (X.L.); pengwei@csust.edu.cn (W.P.); yuanzhihui@csust.edu.cn (Z.Y.)
2   Hunan Key Laboratory of Remote Sensing of Ecological Environment in Dongting Lake Area, Changsha 410114, China
3   School of Traffic and Transportation Engineering, Changsha University of Science & Technology, Changsha 410114, China
4   School of Electrical and Information Engineering, Changsha University of Science & Technology, Changsha 410114, China
5   School of Geosciences and Info-Physics, Central South University, Changsha 410083, China; yangzf@csu.edu.cn
*   Correspondence: lifu_chen@csust.edu.cn

Abstract: Deformation prediction for a salt solution mining area is essential to mining environmental protection. The combination of Synthetic Aperture Radar Interferometry (InSAR) technique with Probability Integral Method (PIM) has proven to be powerful in predicting mining-induced subsidence. However, traditional mathematical empirical models (such as linear model or linear model combined with periodical function) are mostly used in InSAR approaches, ignoring the underground mining mechanisms, which may limit the accuracy of the retrieved deformations. Inaccurate InSAR deformations will transmit an unavoidable error to the estimated PIM parameters and the forward predicted subsidence, which may induce more significant errors. Besides, theoretical contradictory and non-consistency between InSAR deformation model and future prediction model is another limitation. This paper introduces the Coordinate-Time (CT) function into InSAR deformation modeling. A novel time-series InSAR model (namely, CT-PIM) is proposed as a substitute for traditional InSAR mathematical empirical models and directly applied for future dynamic prediction. The unknown CT-PIM parameters can be estimated directly via InSAR phase observations, which can avoid the error propagation from the InSAR-generated deformations. The new approach has been tested by both simulated and real data experiments over a salt mine in China. The root mean square error (RMSE) is determined as ±10.9 mm, with an improvement of 37.2% compared to traditional static PIM prediction method. The new approach provides a more robust tool for the forecasting of mining-induced hazards in salt solution mining areas, as well as a reference for ensuring the environment protection and safety management.

Keywords: InSAR; mine; land subsidence; time series deformation; model

1. Introduction

By the end of 2018, the reserves of mirabilite deposits in China had reached up to 117.297 billion tons [1]. For mirabilite production in the salt mining deposits, water-soluble exploitation, with comprehensively multi-propulsion through groups of drilling wells, is the primary mining mode in salt solution mining area. Attributing to the multi-direction of water-soluble mining activities, the upper layer of the rock salt cavern is prone to overburden, or even serious collapse [2]. As long as the roof of the cavern uplifts to the ground surface, a large pit, which may cause potential damage to the nearby

infrastructures, will be formed [3]. In addition, accumulated water-soluble mining activities may cause significant lithological changes of the underground rock, even inducing a serious pumping of brine and water salinization. Therefore, long-term spatio-temporal deformation prediction of salt solution mines are of considerable importance to the environmental protection and safety management. The multi-temporal interferometric synthetic aperture radar (MT-InSAR) is an advanced space-to-earth observation technology developed in recent years. Compared with traditional InSAR technology, MT-InSAR technology has been reported to be more effective and applicable for deriving ground deformations (i.e., mining area or infrastructures) [4–13]. However, the single MT-InSAR has a limitation in that it can only obtain the deformation sequences during SAR acquisition dates; the subsequent future displacement beyond the span of the SAR observations cannot be acquired. To compensate for the limitation, researchers have incorporated InSAR deformation observations into the Probability Integral Method (PIM), which has successfully solved the problems, such as surface deformation space calculation and overlying strata movement prediction [14–22]. The basic idea for those studies is firstly using the traditional MT-InSAR technique to generate the line-of-sight (LOS) deformation results as input dataset to estimate the PIM parameters; then, the corresponding subsidence sequences for the future period can be predicted based on the PIM prediction model. Those researchers have successfully retrieved the spatio-temporal deformation characteristics and achieved the forward prediction of mining-induced deformations, which proves that the combination with PIM theory is an efficient and feasible complementation to single MT-InSAR technique.

However, there still exist limitations: Firstly, according to previous studies, pure empirical mathematical models (i.e., linear model or linear model combined with periodical function) are mostly utilized to generate the InSAR observations, and the underground mining subsidence mechanism is not considered in the InSAR modeling procedure. In MT-InSAR data processing, the deformation modeling procedure determines the temporal functional relationship between the interferometric phase observations and the parameters. The evolution of mining-induced surface displacement is a complex physical non-linear process, varying with time. Apparently, modeling a physical process with a single empirical mathematical function cannot accurately describe the underground deformation mechanisms and, thus, may have a great impact on the accuracy of the generated InSAR deformation observations. Secondly, inaccurate InSAR deformation results will transmit an unavoidable error to the estimated PIM parameters, then, secondly, propagating to the future subsidence prediction, leading even larger errors in the predicted displacements. Finally, the traditional mathematical models (i.e., linear model or linear model combined with periodical function) used in the deformation monitoring is not consistent with the PIM used in the future deformation prediction, which is based on random medium theory. Using InSAR deformation observations generated via a simple linear model to estimate parameters for a complex non-linear model may not be reasonable. Consequently, contradiction and inconsistency between the InSAR deformation model and the future prediction model is the third limitation.

Based on the above analysis, in order to improve the accuracy of deformation prediction, we propose a novel InSAR deformation model, which can better describe the dynamic evolution disciplines of the underground mining subsidence in the MT-InSAR deformation modeling procedure, as well as be directly used to the forward deformation prediction. The novel model is based on the Coordinate-Time (CT) function (namely CT-PIM) and used as a substitute for traditional InSAR models. CT-PIM improves the static PIM via integrating the temporal parameter to achieve the description of the temporal dynamical characteristics of the mining-induced subsidence. Considering the physical subsurface mechanism, CT-PIM can describe the temporal dynamical characteristics of the mining-induced subsidence more realistically. The PIM parameters are introduced into InSAR time-series phase functions and can be estimated via the phase observations, which can avoid the secondary error propagation from the inaccurate InSAR deformations to the subsequent deformation prediction. Subsidence can be predicted directly based on CT-PIM, which implements in

opposition to the deficiency of inconsistency and lack of reasonability between the InSAR model and the forward prediction model. Consequently, the new method is expected not only to enrich the time series InSAR modeling theory but also provide a more robust tool for forecasting mining-induced hazards in mining areas.

2. Materials and Methods

The CT-PIM, including the Coordinate-Time function, and the PIM parameters are introduced in Section 2.1. The InSAR modeling based on CT-PIM is derived in Section 2.2, together with the final functional relationship between the time series phase observations and the PIM parameters.

2.1. Dynamic Coordinate-Time Probability Integration Model

The Coordinate-Time (CT) function was proposed in Reference [23], which improved the traditional static PIM with introducing the temporal parameter t, thus being referred as CT-PIM hereinafter. It has proven to be effective and reliable in the application for the dynamic ground deformation prediction caused by mining activities. The surface subsidence described in CT-PIM function is as follows [23]:

$$W\ (x,\ y,\ t) = \frac{1}{w_0} W\ (x,\ t) W\ (y,\ t), \tag{1}$$

where $(x,\ y)$ denotes the coordinate of the surface point, and $W\ (x,\ y,\ t)$ is the surface vertical subsidence related to mining activities at time t; w_0 is the maximum settlement, which can be written as $w_0 = mq \cdot cos\alpha$, where m is the thickness of the mine, q is the subsidence factor, and α is the dip angle of the layer. $W\ (x,\ t)$ and $W\ (y,\ t)$ can be expressed as follows:

(1) When the dip direction of the working face is under critical extraction, whereas the strike is under subcritical extraction. This happens in the practical condition that the advancing distance is longer than the depth along the dip direction. The ground subsidence can be written as (the schematic diagram is shown as Figure 1b) [23]:

$$W(x,t) = \begin{cases} \frac{w(x)}{2}\left[erf\left(\sqrt{\pi}\right) + erf\left(\sqrt{\pi}\frac{v_m t - nH - r}{r}\right)\right] \\ \qquad\qquad x \le nH \\ \frac{w(x)}{2}\left[erf\left(\sqrt{\pi}\right) + erf\left(\sqrt{\pi}\left[\frac{v_m t - r - x + \frac{H}{a+bx} - \frac{H(a+bx)}{3}}{r}\right]\right)\right] \\ \qquad\qquad nH <\ x\ < 1.3r \\ \frac{w_0}{2}\left[erf\left(\frac{\sqrt{\pi}}{r}\right) + erf\left(\sqrt{\pi}\frac{v_m t + H/tan\omega - 2x}{r}\right)\right] \\ \qquad\qquad 1.3r \le x \end{cases}, \tag{2}$$

where $w(x)$ can be calculated based on the principles of static PIM following the equation: $w(x) = \frac{w_0}{2}\left[erf\left(\sqrt{\pi}\frac{x}{r}\right) + 1\right]$; erf is a probability integral function: $erf(\frac{\sqrt{\pi}}{r}x) = \frac{2}{\sqrt{\pi}}\int_0^{\frac{\sqrt{\pi}}{r}x} e^{-u^2}\mathrm{du}$ (where u is the integral parameter, r is the main influence radius, $r = \frac{H}{tan\beta}$; H is the mining depth and $tan\beta$ is the tangent of the main influence angle); nH is the starting distance, describing the advancing distance of the working face when the ground point starts to move; n is the starting factor; ω is the static leading influence angle (in degrees); v_m is the mining advancing speed; and the coefficients a and b can be expressed as $a = \frac{117r - \omega nH}{1.3r - nH}$ and $b = \frac{\omega - 90}{1.3r - nH}$, respectively.

(2) When the strike direction of working face is under critical extraction, whereas the dip is under subcritical extraction. This happens in the most practical condition of the coal mining activities, since the strike direction is better to contain a longer advancing distance (even up to several kilometers, much deeper than the depth along the strike),

which can easily satisfy the critical extraction condition. The surface subsidence can be written as (the schematic diagram is shown as Figure 1c) [16]:

$$W(y, t) = \frac{w_0}{2}\left[erf\left(\sqrt{\pi}\frac{y}{r_1}\right) - erf\left(\sqrt{\pi}\frac{y-L}{r_2}\right)\right], \tag{3}$$

where y denotes the vertical coordinate of the ground point in the mining area; r_1 and r_2 represent the main influence radius along the down-dip, and up-dip directions, respectively, which can be expressed as $r_1 = \frac{H_1}{tan\beta_1}$ and $r_2 = \frac{H_2}{tan\beta_2}$. H_1 and H_2 are the mining depths along the down-dip, and up-dip directions, respectively. Here, $H_1 = H - \frac{D_1}{2}sin\alpha$ and $H_2 = H + \frac{D_1}{2}sin\alpha$; L is the estimated length of strike working face, which can be expressed as $L = (D_1 - s_1 - s_2)\frac{sin(\theta_0-\alpha)}{sin\theta_0}$; D_1 is the inclined length of working face; s_1 and s_2 are the offsets of inflection point along down-dip and up-dip directions of the working panel; θ_0 is the mining influence angle, which can be calculated following $\theta_0 = 90° - k\alpha$.
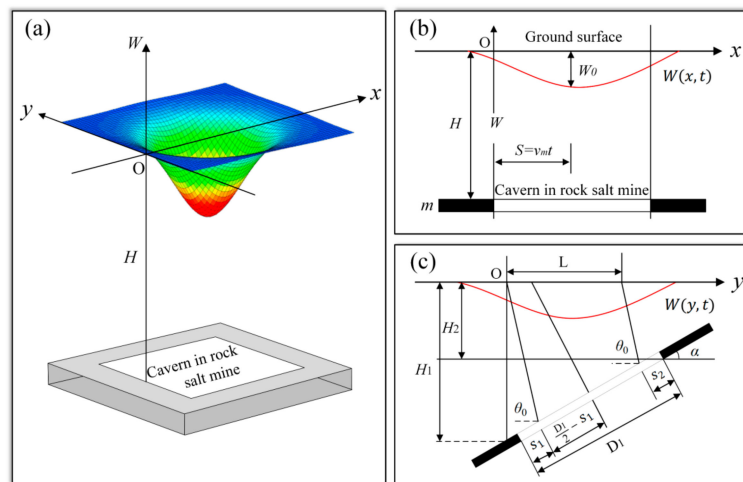

Figure 1. Schematic diagrams for the coordinate system: (**a**) 3D view of the coordinate system; (**b**) profile along strike direction; (**c**) profile along dip direction.

It is worth noting that, when the strike of the working face is under subcritical extraction, the final deformation should be estimated via multiplying a coefficient: $C_{xm} = \frac{W_{xm}}{W_0} < 1$, where $W_0 = mq\cdot cos\theta$. W_{xm} is the maximum value of $W(x, t)$, which can be calculated according to the first equation in Equation (2), under the assumption that the tendency has reached an extreme exploitation [16]. Similarly, when the dip of the working face is under subcritical extraction, then a dip mining degree coefficient, $C_{ym} = \frac{W_{ym}}{W_0} < 1$, should be multiplied with it, where W_{ym} denotes the maximum value of $W(y, t)$ in Equation (3).

2.2. InSAR Modeling Based on CT-PIM (InSAR-CTPIM)

For each high coherence pixel in the *i*-th interferogram [24–26], its corresponding interferometric phase can be expressed as:

$$\delta\varphi^i = \delta\varphi^i_{def} + \delta\varphi^i_{topo} + \delta\varphi^i_{orbit} + \delta\varphi^i_{atm} + \delta\varphi^i_{noise} + \Delta\varphi^i_{non}$$
$$\approx \frac{4\pi}{\lambda}\Delta d^i + \frac{4\pi B_i}{\lambda Rsin\theta}\Delta H^i + \Delta\varphi^i_{res}, \tag{4}$$

where λ is the radar wavelength; Δd is the LOS accumulated deformation spanning the time period of the *i*-th interferogram, referred as the low-pass (LP) component hereinafter; $\Delta\varphi^i_{topo}$ represents the residual topographic phase component; $\Delta\varphi^i_{topo} = \frac{4\pi B_i}{\lambda Rsin\theta}\Delta H^i$, where B_i defines the perpendicular baseline, θ the incident angle, R the sensor-target distance, and ΔH the residual elevation, which is an unknown parameter; $\Delta\varphi^i_{res}$ denotes the final

residual phase, which includes the phase noise, atmospheric delay, and the high-pass (HP) deformation component [27].

During the extraction of the brine from the wellhead, the deformation of the surface caused by the change of the top pressure in the cavern is dominantly along the vertical direction. Besides, the upper dissolution rate of the drilling solution mining process is approximately twice of the side dissolution rate [28]. Therefore, compared with the vertical subsidence, the horizontal displacement caused by water-soluble mining is relatively minor, and omitted hereinafter. Then, the functional relationship between the LOS deformation and the ground subsidence can be expressed as:

$$\Delta d^i = d_{LOS}\left(t_B^i\right) - d_{LOS}\left(t_A^i\right) = [W\left(x,\ y,\ t_B\right) - W\left(x,\ y,\ t_A\right)] \cdot cos\theta, \tag{5}$$

where $W\left(x,\ y,\ t_B\right)$ and $W\left(x,\ y,\ t_A\right)$ are the corresponding dynamic subsidence at t_B and t_A, respectively. Substituting Equation (5) into (4), the functional relationship between the InSAR phases and PIM parameters can be written as:

$$\delta\varphi^i = \frac{4\pi}{\lambda}[W\left(x,\ y,\ t_B\right) - W\left(x,\ y,\ t_A\right)] \cdot cos\theta + \frac{4\pi B_i}{\lambda Rsin\theta}\Delta H^i + \Delta\varphi_{res}^i, \tag{6}$$

where the geological parameter $GP = [m,\ \alpha,\ H,\ D_1,\ \omega]$ of the rock salt mine can be determined according to the in-situ investigation of the study area or the materials provided by the mining company, which can be regarded as known parameters. The unknown parameters to be solved here are $UP = [q, tan\beta,\ s_1,\ s_2,\ k,\ n]$. Among them, q is within the range of [0.01, 1], $tan\beta$, $tan\beta_1$, and $tan\beta_2$ are all distributed within the range of [1, 3.8], and both s_1 and s_2 are within the range of [0.05H, 0.3H]. The propagation influence angle of mining is $\theta_0 = 90° - k\alpha$. Here, k ranges from 0.5 to 0.8, and the starting distance coefficient n ranges from 1/7 to 1/2 [14,16,23]. Equation (6) describes the temporal functional relationship between the InSAR time series phases and the PIM parameters, which is referred as InSAR-CTPIM, and will be applied for the time series deformation generation.

2.3. CT-PIM Parameters Estimation Based on InSAR Phases

If $N+1$ scenes covering the whole study area are acquired at dates $(t_0,\ t_1,\ \ldots,\ t_N)$, then M differential interferometric pairs are generated accordingly. For each pixel $(x,\ y)$ on the differential interferograms, M InSAR functions (in Equation (6)) based on the phase observations can be established. If M is higher than six, the unknown parameters $UP = [q, tan\beta,\ s_1,\ s_2,\ k,\ n]$ can be estimated. The ill-conditioned nature of the phase functions (introduced as Equation (6)) has also been tested to ensure the robustness. For each pixel $(x,\ y)$ on the differential interferograms, M InSAR functions based on the phase observations can be established. The condition number $Cond_\infty(A) = ||A||_\infty ||A^{-1}||_\infty$ is estimated as 18 here, where A defined the coefficient matrix of the phase functions. The value of $Cond_\infty(A)$ implies that no ill-conditioned phenomenon exists in the functions.

The solving of Equation (6) is obviously a non-linear parameter estimation problem. The Genetic Algorithm (GA), combined with the Simplex Method (SM), is introduced here to estimate UP. GA processes the advantages of global optimization searching ability and unrestricting to different model forms [29], and it has been proven to be feasible in solving the problems of non-linear parameter estimation [30]. It generates the optimized estimations in form of population individuals following the principle of fitness function minimization [31]. However, the disadvantages of slow convergence speed and low accuracy are also prominent for GA. SM has proven to be an efficient tool in solving the non-linear estimation problems when combined with GA, which can refine the GA generated results effectively [32]. Consequently, the combination of GA and SM, namely GASM, is adopted here to effectively estimate the unknown parameters.

As for Equation (6), each individual gene is $UP = [q, tan\beta,\ s_1,\ s_2,\ k,\ n]$, and the fitness function here is:

$$f = \left|\left|\Delta\varphi_{res}^i\right|\right| = min, \tag{7}$$

where $\Delta\varphi_{res}^{i}$ denotes the residual phase in Equation (6). After the iteration of population selection, crossing over, and evolution for each individual gene until the minimum fitness function value condition is satisfied, the final obtained individual genes, which are treated as the initial GA-solutions for PIM parameters, will be taken as the input initial values of SM. Then, SM is utilized to improve the accuracy of GA estimations after the global searching, and the corresponding SM-output results are determined as the final solutions for PIM parameters [33].

2.4. Flow Chart and Processing Steps

Figure 2 displays the processing flow of deformation prediction using the CT-PIM function. The steps are as follows:

1. Differential Interferometry according to the $N + 1$ SAR images covering the study area.
2. High-coherent candidates extraction considering both the average coherence and the amplitude dispersion index.
3. InSAR modeling following the CT-PIM function, which establishes the functional relationship between InSAR phases and unknown PIM parameters.
4. PIM parameter estimation based on Genetic Algorithm and Simplex Method (GASM) [32,33], which includes GA global searching to generate the initial values of PIM parameters and SM to optimize the GA solutions.
5. Forward dynamic subsidence prediction beyond the spans of SAR acquisitions based on CT-PIM function introduced as Equation (1).
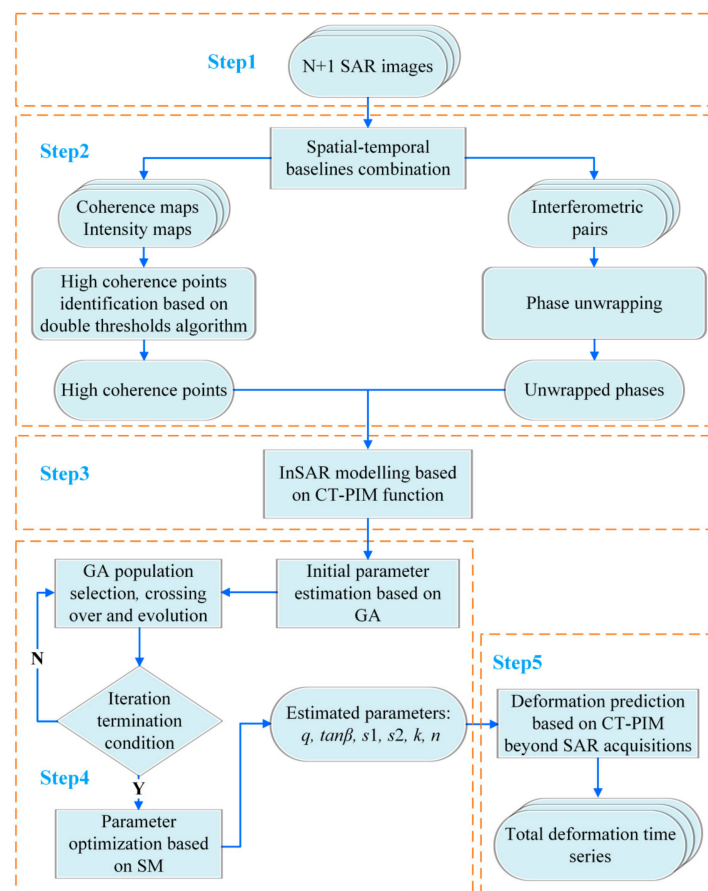

Figure 2. Flow chart of deformation prediction based on CT-PIM function.

3. Results

3.1. Simulated Experiment

A simulated experiment was designed and executed to evaluate the feasibility and accuracy of the proposed method. Satellite parameters used in the simulated experiment were set according to Sentinel-1 A spaceborne parameters, which was to keep consistent with the real data experiment. The geological parameters m, α, H, D_1, ω of the strata overlying the saline layer were set as 0.66 m, 4.5°, 600 m, 300 m, 80° according to real data collected by the company in charge of the mining activity in the area. The advancing speed v_m at the simulated experiment was set as 0.24 m/d, which was also according to the real data (will be discussed in Section 3.2.1). The simulated true values of *UP* were set primarily as 0.504, 1.560, 30.310 m, 16.080 m, 0.524, 0.167.

After setting those parameters, the time series settlement field could be generated according to Equation (1), which would be used as the real settlement field compared with the subsidence generated based on the InSAR-CTPIM processing. The selected images of the simulated real settlement field are shown in Figure 3. InSAR phase functions can be simulated according to Equation (6), and the residual elevation ΔH was simulated via Gaussian random simulator with its magnitude within $[-20, 20]$ m. The random noise with a variance from 0 rad to 0.65 rad was added in the simulation. The random noise we added here can be expressed as $Noi = sqrt\,(0.65)\,*\,randn\,(60, 60)$, where *Noi* represents the noise; $sqrt\,(0.65)$ represents the variance of 0.65 rad; *randn* is the random noise function in MATLAB; and $(60, 60)$ is total simulated size of the phase function. Totally, 600 indexes of pixels were randomly extracted for the subsequent quantitative comparison with the CT-PIM generated deformation. In order to evaluate the impacts of different numbers of interferometric pairs on the corresponding generated deformation results, the simulation experiments with a multi-master connection were designed [34]. Six subgroups of simulation were carried out, with the number of interferometric pairs as 10, 15, 20, 25, 30, and 35, respectively, which also represented the number of InSAR phase functions. The corresponding GASM procedure was performed to obtain the CT-PIM parameters based on the simulated InSAR phase observations, and the final estimated subsidence could be obtained via Equation (1). The parameters, such as the spatio-temporal baselines, used in the simulation were set according to the real data experiment (in Section 3.2.2).
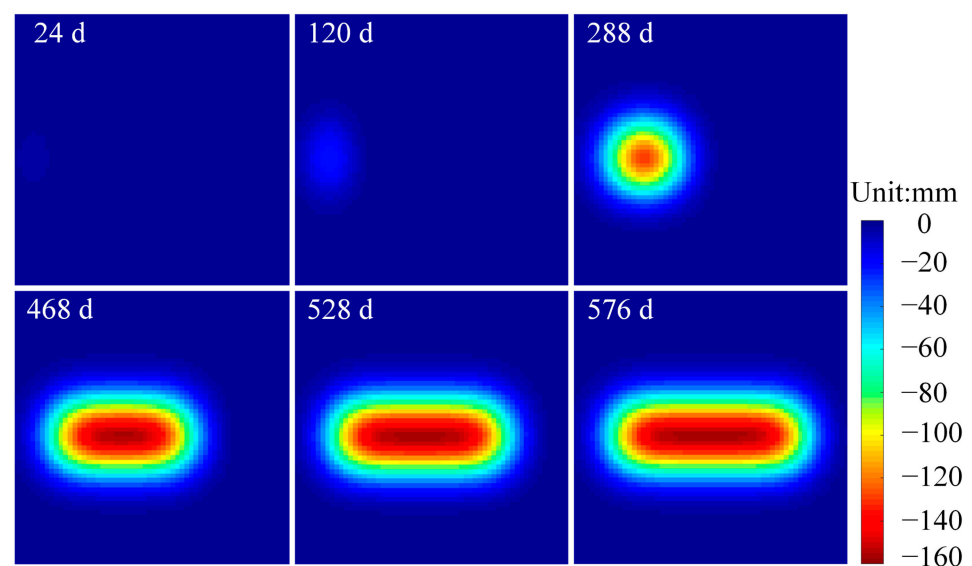

Figure 3. Selected images of simulated settlement field (at 24 d, 120 d, 288 d, 468 d, 528 d, and 576 d, respectively).

To estimate the unknown parameters of CT-PIM, the maximum iteration number, the population size, the crossover probability, and the mutation probability in GASM algorithm

were set as 400, 60, 0.5, and 0.2, empirically. After the SM secondary optimization, the final optimal estimations of the CT-PIM parameters could be generated for each subgroup of simulation. Substituting the obtained parameters into Equation (1), the time series settlement field could be generated.

Figure 4 illustrates the relative errors for each parameter between the CT-PIM generated values and the simulated real ones under a different number of interferometric pairs. The lower the relative error is, the higher is accuracy suggested for the CT-PIM estimated parameter. As can be seen from the figure, generally, the relative errors decrease with the increase of interferometric numbers. Under a multi-master connection, a stack of 20 interferograms is acceptable in our cases. It can also be noted from Figure 4 that, among the six parameters, q and $tan\beta$ were more sensitive with higher curvature slopes than the remaining four parameters.
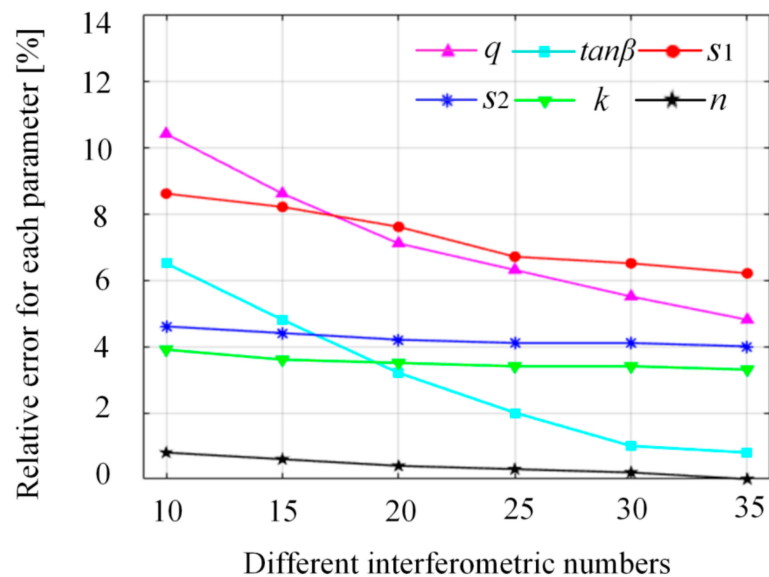

Figure 4. Relative errors with different interferometric numbers under multi-master connection.

We extracted the interferometric pairs of 10 and 35, respectively, to show a quantitively comparison with the simulated real values (shown as Tables 1 and 2). The results show that the use of 35 interferometric pairs under the multi-master connection to estimate the unknown parameters is evidently more accurate (for instance, the relative error for q is only 4.8% under 35 pairs compared with that of 10.4%). Therefore, we finally determined to use 35 interferometric pairs (noise level with a variance of 0.65 rad) under the multi-master connection in the real data experiment. It can also be noted that, among the six parameters, the relative error of s_1 is relatively large, both in Tables 1 and 2, with 8.6 % and 6.2%, respectively. This is consistent with the results of the sensitivity analysis in Section 3.3.3.

Table 1. Estimated CT-PIM parameters (under the 10 interferometric pairs).

Parameters	Simulated Real Value	CT-PIM Generated Value	Error	Relative Error
q	0.504	0.559	0.055	10.4
$tan\beta$	1.560	1.662	0.102	6.4
$s_1(m)$	30.310	27.801	2.509	8.6
$s_2(m)$	16.080	15.340	0.740	4.5
k	0.524	0.504	0.020	3.9
n	0.167	0.166	0.001	0.6

Table 2. Estimated CT-PIM parameters (under the 35 interferometric pairs).

Parameters	Simulated Real Value	CT-PIM Generated Value	Error	Relative Error
q	0.504	0.528	0.024	4.8
$tan\beta$	1.560	1.572	0.012	0.8
$s_1(m)$	30.310	28.431	1.879	6.2
$s_2(m)$	16.080	15.437	0.643	4.0
k	0.524	0.507	0.017	3.3
n	0.167	0.167	0	0

Figure 5 shows the comparison results between the selected time series settlement generated by CT-PIM and the simulated settlement with 600 pixels (35 interferometric pairs, multi-master connection, with a noise variance level of 0.65 rad), and the differences are illustrated in Figure 5f in red polylines. It can be noted that the two groups of results demonstrate good agreement even under a relatively high noise level of 0.65 rad, and the max deviation increases with the time span. According to the quantitative statistics for Figure 5a–f, the number of points with the deviations within [−5, 5] mm account for 100%, 100%, 97%, 90%, 87.6%, and 85.8% of the total number of points for spans of 24 days, 120 days, 288 days, 468 days, 528 days, and 576 days, respectively, and the corresponding maximum deviation is 0.1 mm, 1.3 mm, 7.9 mm, 9.3 mm, 9.5 mm, and 9.6 mm, respectively. Compared with the maximum subsidence for each period (i.e., 165 mm at 576 days), the deviation was relatively minor (a 9.6 mm deviation occupy only 5.8% approximately). To quantitatively evaluate the distribution of the deviations, statistical analysis for the probability distribution was carried out. Figure 6 demonstrates the probability distribution of the average deformation deviations with 600 pixels. As determined, the magnitudes of errors are concentrated within a relatively low ranges, with 83.8% of points distributed within [−2, 2] mm and all the pixels distributed within [−6, 6] mm, which implies that the proposed method is of promising accuracy. The RMSE between the CT-PIM generated value and the simulated real settlement is estimated as ±4.5 mm.
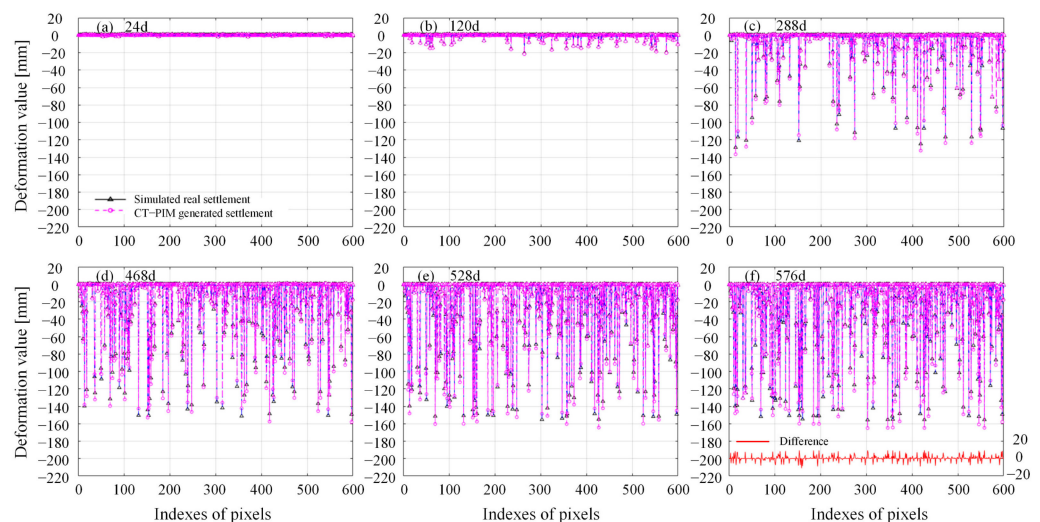
Figure 5. Comparison between the CT-PIM generated deformation sequences (six periods are selected) and the simulated real settlement.
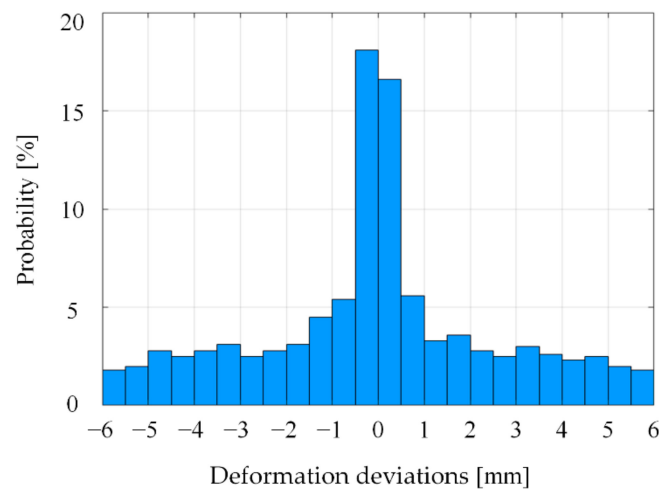
Figure 6. Probability distribution for deformation deviations.

3.2. Real Data Experiment

3.2.1. Study Area and SAR dataset

A salt mine, located in China, was selected as the study area. Figure 7 displays the location of our test area in Hunan Province and the corresponding coverage of SAR satellite images. The red rectangle in Figure 7b represents the spatial coverage of Sentinel-1 A image obtained by a satellite ascending geometry, and the purple rectangle represents the area of interest. The mine is located in the central part of Liyang Plain, with the characteristics of abundant natural water systems, numerous large and densely distributed ponds, crisscrossing artificial channels, and extensive surface paddy fields. Long-term drilling soluble mining activities have caused serious land salinization, which imposed significant influences to the surrounding environment (see Figure 8a). The mining-induced accumulated subsidence also led to cracks on the ground surface of roads, which imposed potential damage to infrastructures built on the nearby residential area (see Figure 8b,c). Gradually accumulated ground subsidence may also generate an obvious stagnant water pit (shown as Figure 8d, with a settlement approximately of 1.5 m).
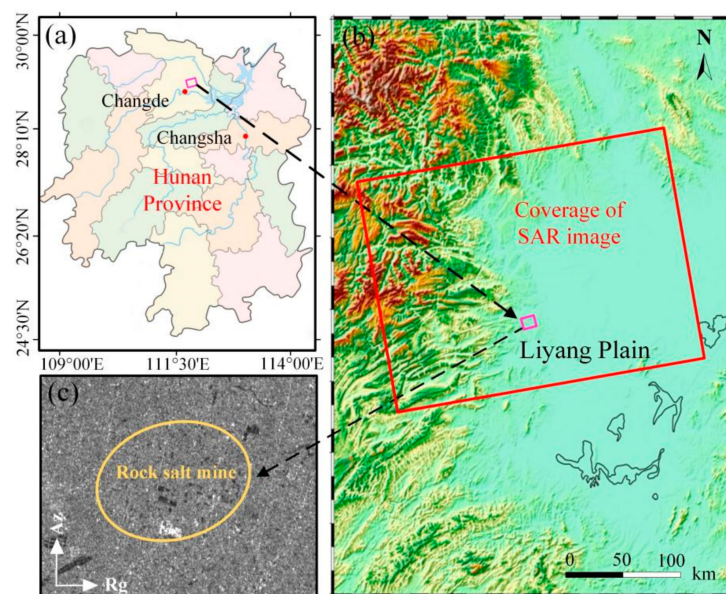

Figure 7. Study area and SAR spatial coverage: (**a**) map of Hunan Province; (**b**) coverage of SAR images; (**c**) mean amplitude image of the study area.
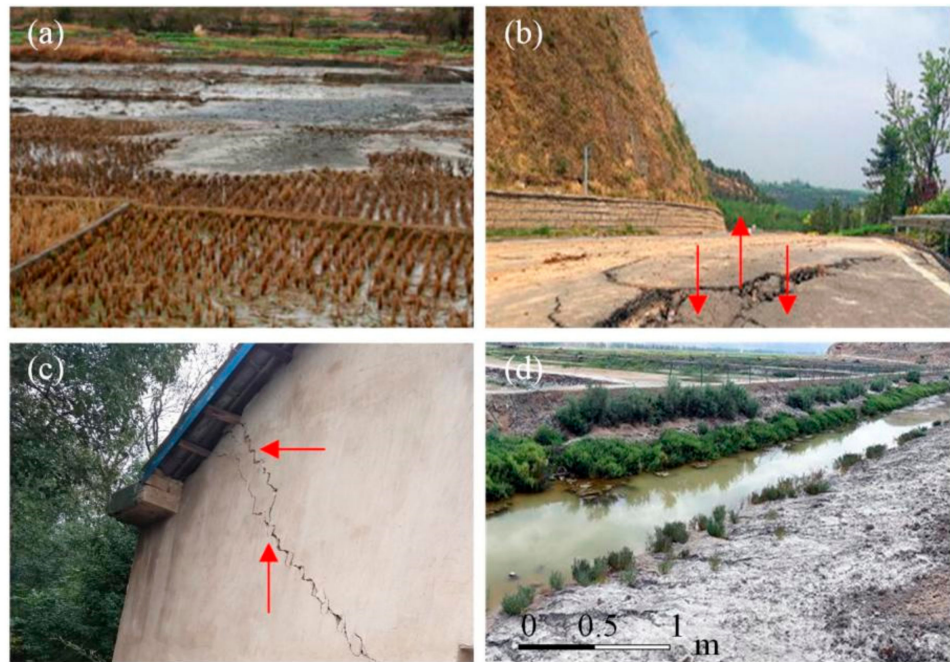
Figure 8. Field pictures of the residential area near the study area: (**a**) area with land salinization; (**b**) uneven displacement on the road; (**c**) cracks on the wall of a house; (**d**) a water pit in the salinized area.

Figure 9 shows the local geological asset. The underground stratums mainly include Lower Tertiary and Quaternary. The lithological components over this area mainly consist of mudstone, dolomite, siltstone, gypsum, mirabilite, and glauberite. Anhydrous Glauber salt (Na_2SO_4, 62.76–78.8%) produced in this area exist in the salt-bearing section (E_2x^3) of Neogene Formation. Argillaceous dolomitic mirabilite is the dominate lithological component, which distributes over the up layer, bottom layer, and interlayer and belongs to weak layered rock mass. The poor stability of the rocks in this area makes the ground surface vulnerable to soften and collapse.
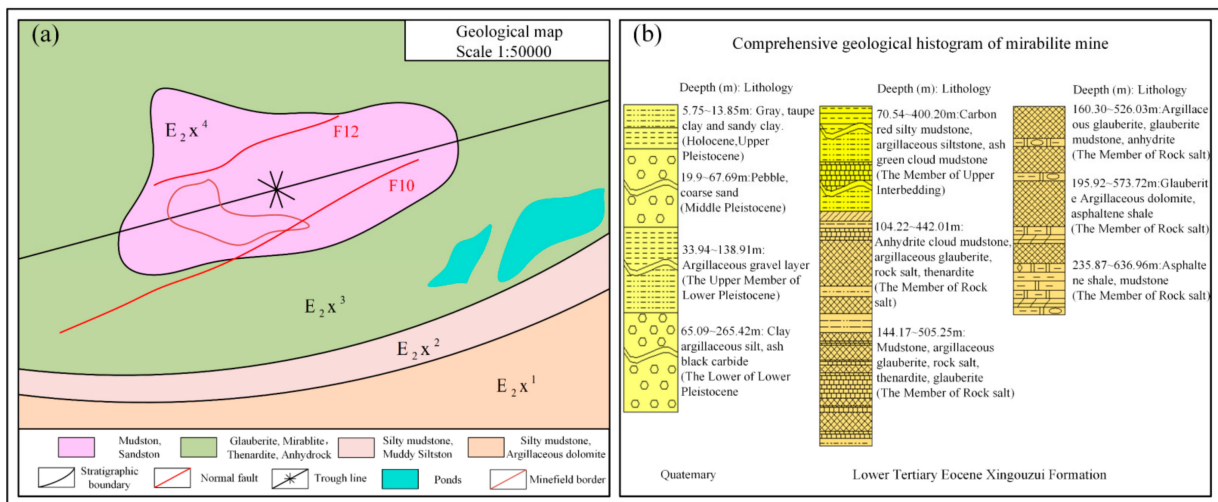

Figure 9. Schematic diagram of the lithological distribution over the study area.

According to the above lithological characteristics of the upper layer on the working surface and the collected geological materials of the mine, the aforementioned lithologic

geological parameters *GP* (see Table 3) is set as $GP = [3\,\text{m}, 5.7°, 240\,\text{m}, 258\,\text{m}, 80°]$ according to the geological materials provided by the mining company. The advancing speed v_m is practically calculated according to properties of the sedimentation funnel in the mining area, which follows the equation $v_m = \frac{S}{t} = 0.056\,\text{m/day}$, where S denotes the mean radius for the sedimentation funnels, and t denotes the time span of the mining activities.

Table 3. Geological parameters.

Geological Parameters	*m* (m)	α (°)	*H* (m)	D_1 (m)	ω (°)	v_m (m/Day)
value	3	5.7	240	258	80	0.056

3.2.2. SAR Data Acquisition and Preprocessing

A total of 32 Sentinel-1A scenes with ascending geometry spanning the period from 15 June 2015 to 15 August 2017 were collected for the differential interferometric dataset processing. The unwrapped interferometric pairs with small spatial-temporal baselines were generated via SARScape 5.2 and ENVI 5.3. The SAR sensor parameters and spatial-temporal baselines are shown in Table 4 and Figure 10, and the subsequent high coherence points extraction, InSAR deformation modeling, CT-PIM parameter estimation, and deformation generation were all executed via MATLAB software. In the preprocessing of differential interferometry, the multi-look ratio of SAR image was set as 5:1, with the sampling resolutions as 9.022 m along azimuth, and 7.368 m along range direction, respectively. Spatial-temporal interferometric baselines were set lower than 150 m and 420 days, respectively, with all the images registered and resampled to a super master image (acquired at 3 July 2016). External 30 m resolution Shuttle Radar Topography Mission Digital Elevation Model (SRTM DEM) data was used to filter the terrain phase [35]. The procedure of phase unwrapping was executed with the Minimum Cost Flow (MCF) method. After artificially eliminating the unsatisfied interferometric pairs with poor unwrapping effect, totally, 58 unwrapped differential interferograms were generated [36,37]. Thresholds for moderate to high coherent points were set as 0.45 for coherence, and 0.35 for mean amplitude dispersion index. Finally, a total of 6027 candidates in the mining area were extracted.
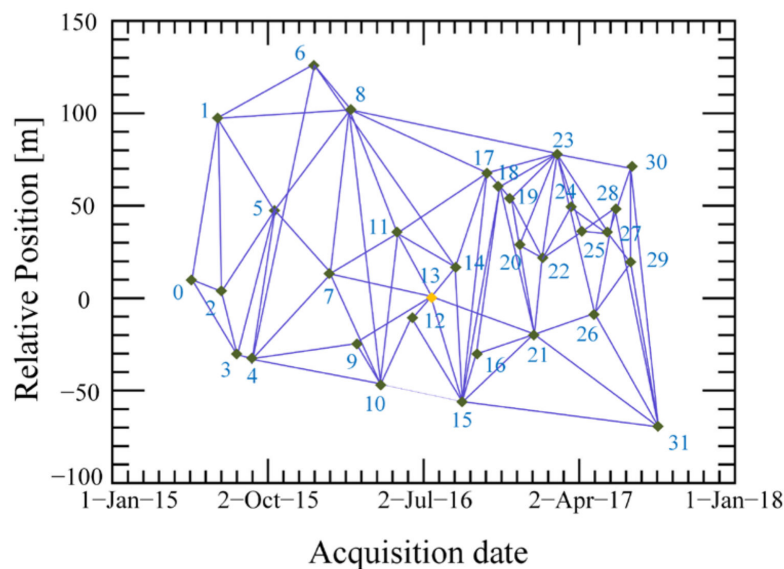

Figure 10. Spatio-temporal baselines.

Table 4. Interferometric pairs and sensor parameters (Ascending, Orbit No. 11).

Image No.	Acquisition Date (yyyy/mm/dd)	Perpendicular Baseline (m)	Temporal Baseline (Days)
0	2015/06/15	10.32	−384
1	2015/07/09	94.46	−360
2	2015/08/02	8.65	−336
3	2015/08/26	−25.59	−312
4	2015/09/19	−27.87	−288
5	2015/10/13	42.76	−264
6	2015/12/24	125.03	−192
7	2016/01/17	19.96	−168
8	2016/02/10	99.87	−144
9	2016/03/05	−21.75	−120
10	2016/03/29	−48.25	−96
11	2016/04/22	37.12	−72
12	2016/05/16	−9.33	−48
13	2016/07/03	0	0
14	2016/08/20	15.15	48
15	2016/09/25	−54.32	84
16	2016/10/07	−27.33	96
17	2016/10/19	63.93	108
18	2016/10/31	57.18	120
19	2016/11/12	52.15	132
20	2016/11/24	26.62	144
21	2016/12/18	25.12	168
22	2016/12/30	20.94	180
23	2017/01/11	76.93	192
24	2017/02/16	48.78	228
25	2017/03/12	34.61	252
26	2017/04/05	−16.41	276
27	2017/04/29	34.59	300
28	2017/05/23	47.07	324
29	2017/06/28	16.92	360
30	2017/07/22	63.26	384
31	2017/08/15	−69.95	408

3.2.3. PIM Parameter Estimation Based on InSAR-CTPIM

Before the novel InSAR-CTPIM processing being applied for the study area, the traditional SBAS-InSAR with multi-linear velocity model was performed to capture the spatial-temporal deformation characteristics over the rock salt mine. As shown in Figure 11, it can also be determined that apparent multi subsidence bowls developed during the observations from a spatial view. This phenomenon is related to drilling water-soluble mining activities. As in situ investigated, the mining mode for the test rock salt mine is multi-well groups connectivity, where more than two wells are connected for each well group during the drilling soluble mining; thus, multi settlement funnels will be formed around each well group. Since the CT-PIM model is based on a single subsidence funnel, it is difficult to accurately cover the whole test area containing complex multi settlement funnels with a single CT-PIM. Consequently, we divided the area into seven sub-settlement funnels, which are shown as Figure 11b, with the subsidence image at 15 August 2017 as the background.
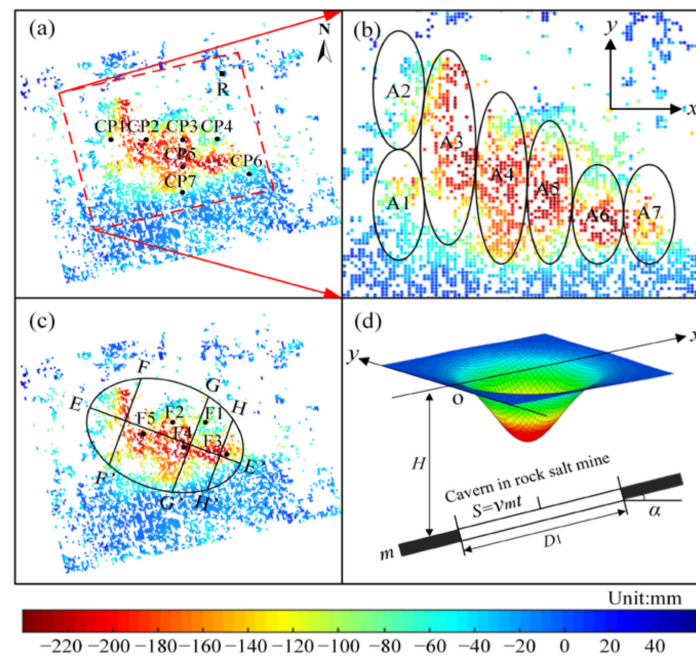
Figure 11. Schematic map of sub-settlement funnels distribution (with the settlement at 15 August 2017 generated via SBAS as the background): (**a**) the leveling points; (**b**) distribution of the seven sub-settlement funnels; (**c**) the distribution of the traverse-longitudinal profiles of the funnels; (**d**) 3D version of the mining coordinate system.

In InSAR-CTPIM processing, 24 images from 15 June 2015 to 11 January 2017 were extracted to estimate the CT-PIM parameters with GASM algorithm, which would be used to generate the corresponding deformation sequences following the step 4 of the procedures introduced in Section 2.4. Based on the obtained CT-PIM parameters, the remaining eight images (from 16 February 2017 to 15 August 2017) were reserved to validate the forward predicted deformation generated by CT-PIM following the step 5. During the GASM procedure, seven sub-funnels were processed separately, with seven groups of parameters generated, which is shown in Table 5.

Table 5. Estimated CT-PIM parameters.

Parameters	A1	A2	A3	A4	A5	A6	A7
q	0.832	0.882	0.919	0.741	0.957	0.750	0.974
$tan\beta$	3.060	3.128	3.473	3.362	3.732	3.608	2.995
$s_1\ (m)$	39.170	40.694	44.933	49.888	42.297	47.468	31.116
$s_2\ (m)$	36.481	38.631	32.001	39.813	48.184	47.374	26.701
k	0.518	0.623	0.743	0.693	0.658	0.702	0.718
n	0.150	0.162	0.182	0.196	0.145	0.193	0.166

3.2.4. Deformation Prediction Based on CT-PIM

Based on the seven groups of obtained CT-PIM parameters in Table 5, the deformation sequences covered by SAR data acquisition can be derived by InSAR-CTPIM. Figure 12 shows the time series deformation generated spanning from 15 June 2015 to 11 January 2017, which were treated as the deformation monitoring results. The deformation beyond SAR data acquisition can be predicted according to CT-PIM (expressed as Equation (1)). Figure 13 shows the eight 3D scenes (from 16 February 2017 to 15 August 2017) of the predicted subsidence based on CT-PIM, which were treated as the deformation prediction results. From 9 July 2015 to 10 February 2016, the overall deformation of the whole area was relatively stable, with the maximum estimated subsidence as only 52 mm. Obvious

subsidence began to occur at 5 March 2016 after an 8-month temporal lag, and the subsiding velocities have increased rapidly since then. Since 20 August 2016, the boundary of the seven sub-settlement bowls has become apparently more distinct, with the maximum subsidence increasing from 110 mm to 205 mm on 11 January 2017. As of 15 August 2017, the maximum subsidence had accumulated up to 294 mm.
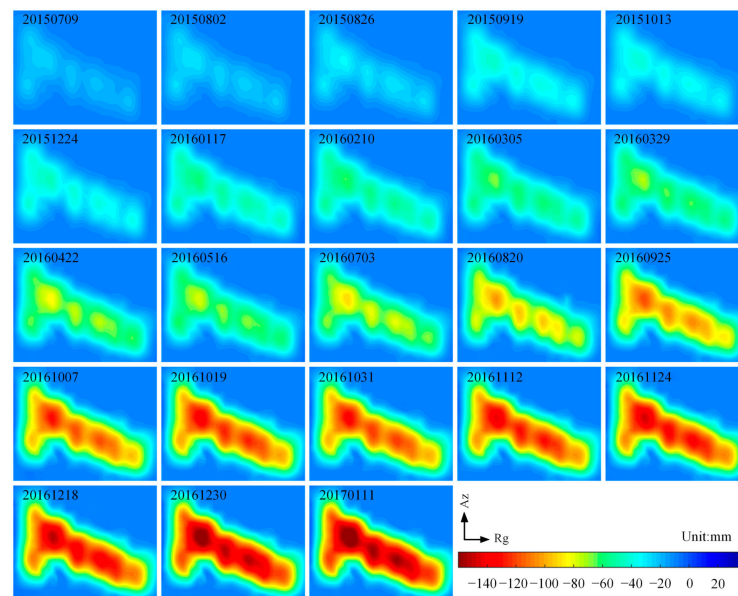

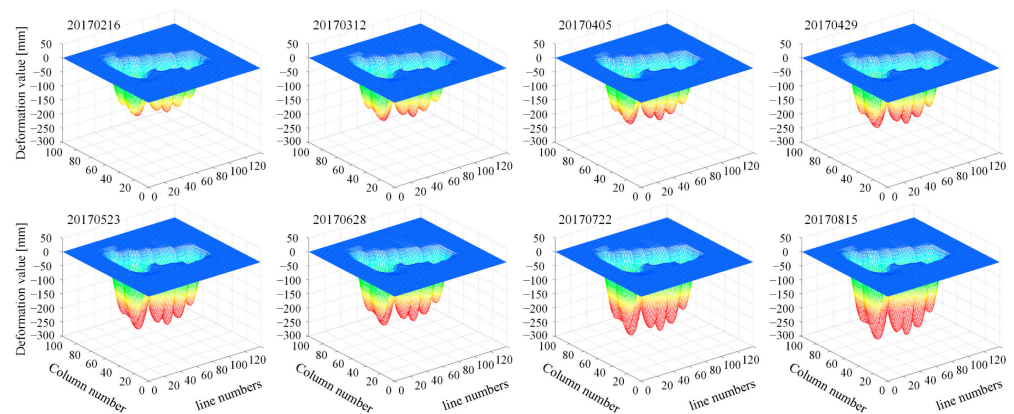**Figure 12.** Derived deformation sequences based on InSAR-CTPIM (reference date: 15 June 2015).

Figure 13. Three-dimensional scenes of the predicted subsidence based on CT-PIM (reference date: 15 June 2015).

3.3. Accuracy Analysis

3.3.1. Accuracy Evaluation for InSAR-CTPIM Monitored Subsidence

The historical leveling measurements from 2 August 2015 to 18 December 2016 for the test mine were collected, which can be used to test the accuracy of the deformation results during the SAR acquisitions obtained by InSAR-CTPIM. The locations of the leveling points (CP1, CP2, . . . , CP7) are marked in Figure 11a, with the reference point marked as *R* in the north-east corner. The leveling measurements which covered consistent periods with the SAR acquisition dates were extracted to conduct a more precise comparison with the InSAR-CTPIM monitored subsidence.

Figure 14 shows the comparison between the results of InSAR-CTPIM, SBAS-InSAR, and leveling measurements. The average RMSE of InSAR-CTPIM results was estimated as ±6.9 mm, whereas that of traditional SBAS-InSAR was ±8.5 mm, with an increase

of approximately 20.8%. It can be determined that the dynamic settlement obtained by InSAR-CTPIM shows better consistency with the leveling measurements. According to our experiment, almost all the leveling points in the mining area were under a considerable subsiding period. The most serious settlement occurred at CP3, with a value of 156 mm. The RMSE accounts for 4.4% of the maximum settlement, which implies the promising accuracy of InSAR-CTPIM in deriving time series subsidence of the rock salt mine.
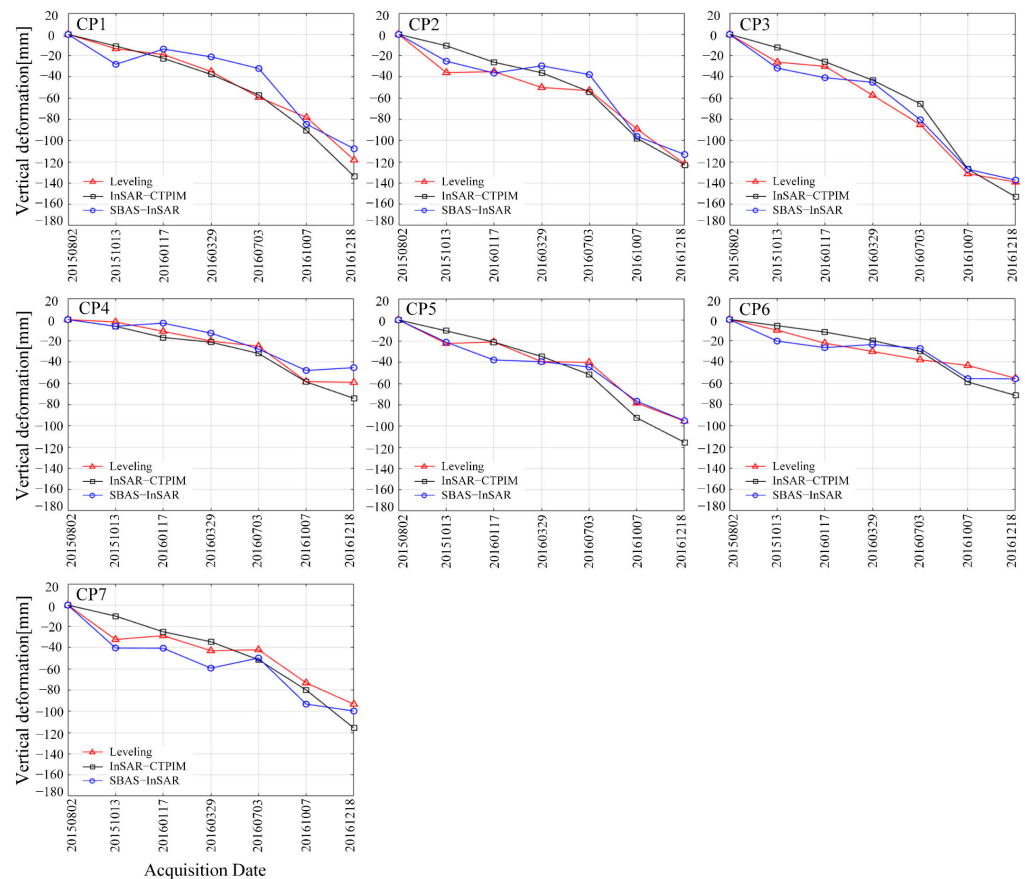

Figure 14. Time series deformation at leveling points (reference date: 2 August 2015).

3.3.2. Accuracy Evaluation for CT-PIM Predicted Subsidence

As discussed above, the remaining eight images from 16 February 2017 to 15 August 2017 were reserved to evaluate the forward subsidence prediction results. To compensate for the unavailability of simultaneous periods of leveling measurements, SBAS-derived results were used to be compared with the predicted subsidence. The traditional static PIM prediction method introduced in References [20,38], which inversed the PIM parameters based on a single interferometric pair, was carried out preliminarily to be compared with the CT-PIM predicted results. Four periods of predicted subsidence (spanning from 15 June 2015 to 26 February 2017, 5 April 2017, 28 June 2017, and 15 August 2017, respectively) were extracted, which is shown as Figure 15. The maximum subsidence predicted via static PIM were relatively lower than those of SBAS-InSAR. On 15 August 2017, the maximum subsidence predicted by static PIM was estimated as 325 mm, with a 39-mm difference with the SBAS-derived result, while the difference of CT-PIM is only 8 mm.
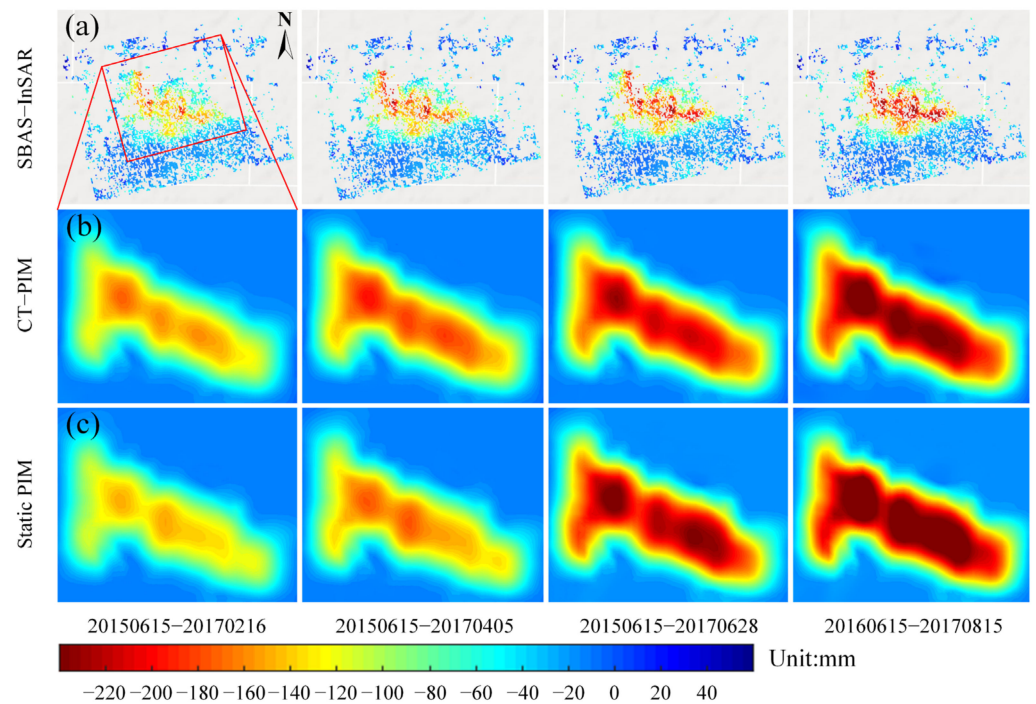
Figure 15. Subsidence comparison: (**a**) SBAS-InSAR results; (**b**) CT-PIM predicted; (**c**) static PIM predicted (with reference to 15 June 2015).

For further quantitative analysis, the points located in the subsidence funnels were extracted from Figure 15. The probability distribution was statistically analyzed, and the distribution histograms are shown as Figures 16 and 17. As Figure 16 shows, the residual errors for all the sampled points between CT-PIM predicted subsidence and those of the SBAS results during the four temporal periods are mainly distributed within the range of $[-25, 25]$ mm. The RMSE is estimated as ±12.8 mm, ±12.7 mm, ±12.9 mm, ±13.2 mm, respectively. In contrast, those residual errors for static PIM (shown as Figure 17) are mainly distributed within a more disperse range of $[-40, 40]$ mm, with its RMSE estimated as ±20.2 mm, ±18.5 mm, ±20.7 mm, ±15.8 mm, respectively, which are much higher. Apparently, the distribution of CT-PIM errors is better concentrated than those of static PIM, which indicates a better consistency with the SBAS technique and a higher predictive accuracy. The total STD of those errors for CT-PIM is estimated as ±12.9 mm. It can be inferred that the CT-PIM predicted results show better consistency with the traditional SBAS-derived subsidence than that of static PIM predicted ones, with an increase of 37.2% compared to that of static PIM.
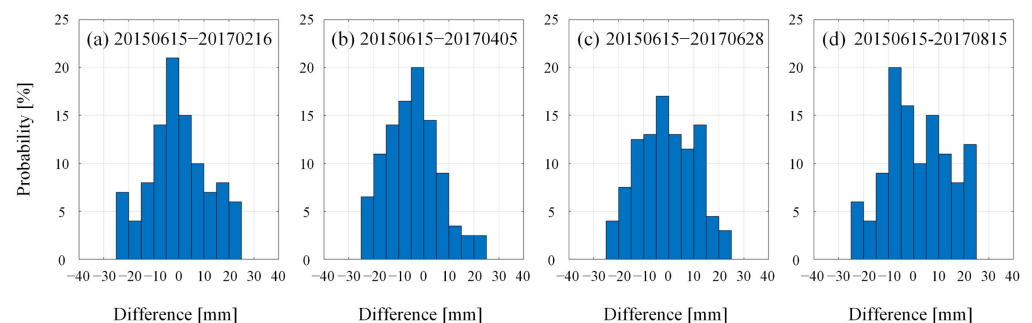

Figure 16. Differences of CT-PIM predicted subsidence with comparison of SBAS-InSAR results (with reference to 15 June 2015).
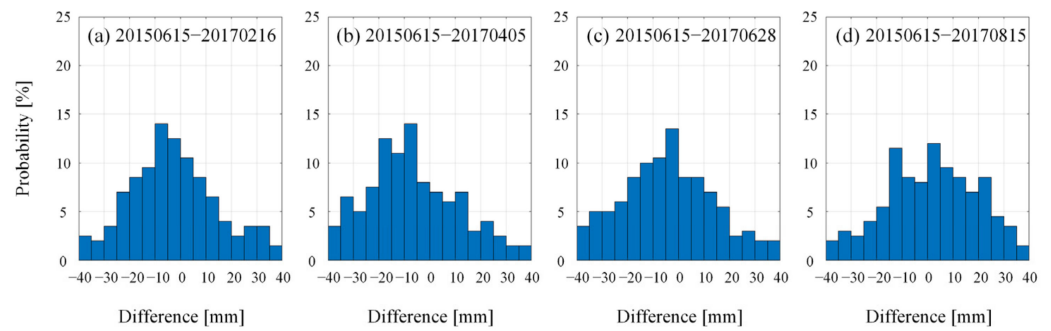
Figure 17. Differences of static PIM predicted subsidence with comparison of SBAS-InSAR results (with reference to 15 June 2015).

3.3.3. Sensitivity Analysis on CT-PIM Parameters

Since CT-PIM is directly used to predict the forward dynamic deformation subsequent to the SAR acquisitions, the accuracy of the predicted mining subsidence directly depends on the accuracy of CT-PIM parameters. Consequently, it is necessary to analyze the sensitivity of CT-PIM parameters. Sensitivity analysis can assist us in understanding how the parameters influence the predicted deformation, i.e., which parameter impacts the most and to what extent it impacts the results. The sensitivity analysis method based on Sobol indices is introduced here to execute a simulated experiment [39].

Sobol indices describe the correlation between each parameter and its global sensitivity on the objective function. The higher the sensitivity index, the higher the result error of the parameter on the deformation. Firstly, the objective function is decomposed based on variance analysis; then, the first-order indices (S_{α}, where α represents the certain parameter) and total-effect indices (S_{α}^{Tot}) of each parameter is calculated, and the sensitivity of the interactive input parameters can also be generated. Here, S_{α} represents the partial variance, which describes the main contribution of a sample of the certain parameter for the output variances, while S_{α}^{Tot} represents the total variance, which describes the percentage of a group of samples for a certain parameter on the output variances. Finally, the disturbance analysis is used to quantitatively analyze the influences of different parameters on the final predicted deformation. The estimated two kinds of indices for each CT-PIM parameter are shown in Figure 18, where X axis represents the input parameters ($UP = [q, tan\beta, s_1, s_2, k, n]$), and Y axis represents the Sobol indices for each parameter. The closer the magnitude of each corresponding Sobol index to 1, the higher sensitivity the parameter possesses. Table 6 lists the ranges of different importance extent. From it, we can determine that all the parameters are beyond the range of "Not correlated", which implies their impacts on the accuracy of predicted deformation cannot be ignored. Among the six parameters, q and $tan\beta$ are more sensitive to the model, with the Sobol indices S_{α}^{Tot} of 0.95 and 0.90, respectively, which can be treated as "Very important" parameters. Consequently, we should pay more attention to the error control during the parameter estimation procedure for those two parameters. In contrast, s_1 and s_2 show relatively lower sensitivity than the remaining four parameters, with the Sobol indices S_{α}^{Tot} of 0.60 and 0.65, respectively. The two parameters can be treated within the united range of "Unimportant" and "Important".

Table 6. Correlation extent for different ranges of sensitivity indices [39].

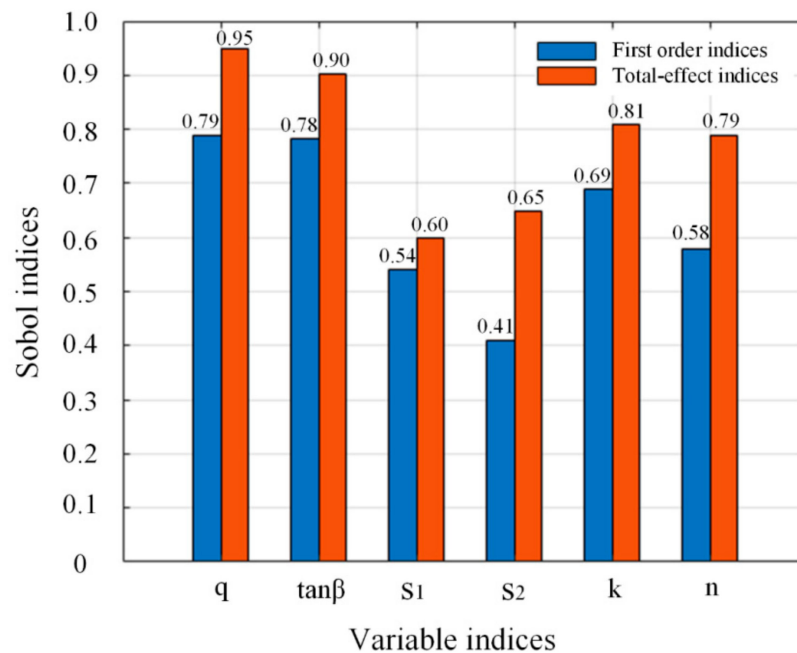| Correlation Extent	Ranges of Sensitivity Indices
Very important	$0.8 < S_{\alpha} < S_{\alpha}^{Tot} \leq 1$
Important	$0.5 < S_{\alpha} < S_{\alpha}^{Tot} \leq 0.8$
Unimportant	$0.3 < S_{\alpha} < S_{\alpha}^{Tot} \leq 0.5$
Not correlated	$0 < S_{\alpha} < S_{\alpha}^{Tot} \leq 0.3$

Figure 18. Estimated Sobol indices for CT-PIM parameter.

4. Discussion

Subsidence along the traverse and longitudinal lines marked in Figure 11c (EE', FF', GG', HH') were extracted for a profile analysis. The profile analysis results based on the SBAS-InSAR derived time series subsidence are shown in Figure 19 (as shown the dotted line), while the CT-PIM results are shown as Figure 19 (as shown the solid line). From the figures, we can see similar spatial-temporal characteristics and approximate same locations of pixels with separate subsidence bowls along EE', FF', GG', and HH', for both the two groups of generated results. The discrepancy between the SBAS results and CT-PIM predicted ones, in the case of Figure 19c (particularly in the black rectangle), was suggested to be related to the following reasons: (1) The systematic uplifts in the black rectangle in Figure 19c for the SBAS results were related to the residual atmospheric delay and orbital errors. During CT-PIM processing, the mining area was divided into several subsidence bowls artificially. (2) We treated the GG' profile that only traversed a single subsidence funnel, and only one group of CT-PIM parameters was used to predict the subsidence. Some unrevealed deformation characteristics maybe hidden in the predicted results, which can be revealed by the SBAS-InSAR monitored results. As we determined for the InSAR-CTPIM derived results, the apparent three peak values were detected at 172 m, 322 m, and 414 m along EE', with the subsidence of 232 mm, 249 mm, and 205 mm, respectively, and peak values at 149 m along the FF' section of 219 mm, whereas, at 172 m, along GG' of 218 mm and, at 80 m, along the HH' of 247 mm. The multi peaks of the subsidence along traverse and longitudinal directions were due to the water-soluble mining activities with groups of drilling wells simultaneously.
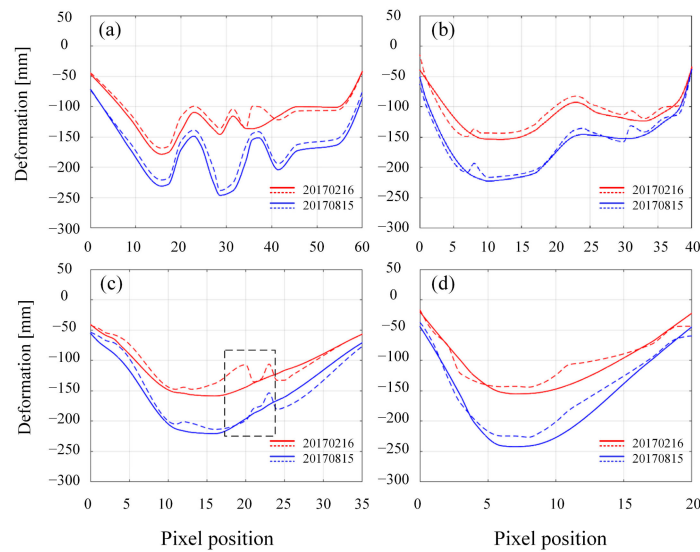
Figure 19. Profile analysis based on SBAS (dotted line) and CT-PIM (solid line) predicted subsidence: (**a**) Profile EE'; (**b**) FF'; (**c**) GG'; (**d**) HH'.

Five feature points (F1–F5, marked in Figure 11c) are extracted for quantitative analysis, and the results are shown in Figure 20. It can be seen from Figure 20 that, during the whole period, the five feature points displayed similar temporal evolution trends: slow settlement period from 15 June 2015 to 29 March 2016, and then a rapid settlement period from 29 March 2016 to 15 August 2017. Maximum subsidence was determined at F5 with its accumulated settlement of 289 mm until 15 August 2017. In contrast, F1, which was far away from the wellhead, was relatively stable, with its maximum deformation accumulated to 98 mm until 15 August 2017. As introduced in Section 3.2.4, an 8-month temporal lag of the subsidence can be found in Figure 20, which is suggested to be mainly related to the dissolution processing of the mirabilite by the solvent, with a certain longer time from injection to the surface displacement emerged. In addition, the depth of rock salt mine is generally deeper than that of common coal mines, which also leads to the time delay from the underground displacement cavity being accumulated on the ground surface.
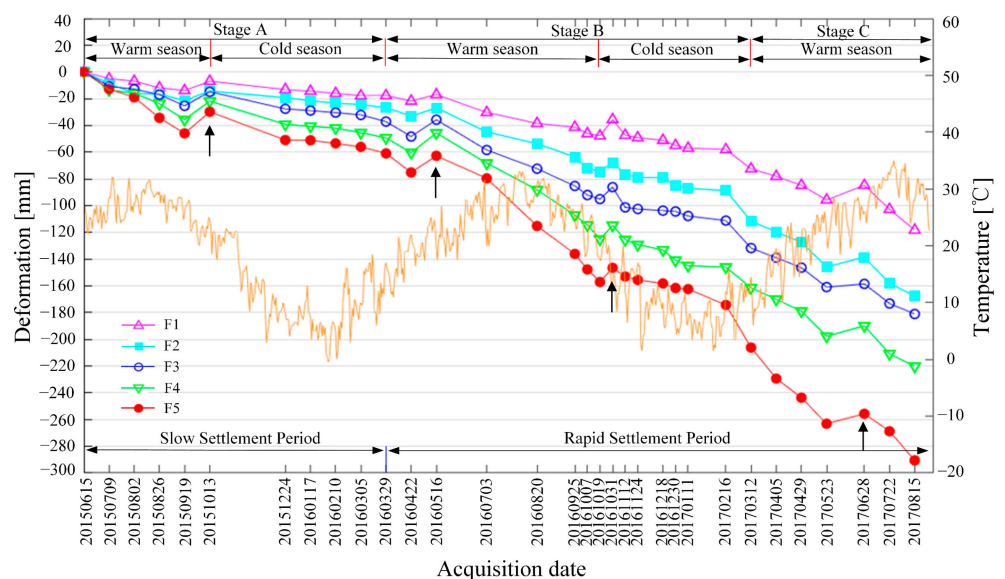

Figure 20. Time series settlement on feature points based on InSAR-CTPIM.

Another phenomenon of seasonal related variations was determined from our experiments. For a warm season (29 March 2016 to 19 October 2016 in Stage B and 12 March 2017 to 15 August 2017 in stage C), a rapid subsiding trend occurred for all the five feature pixels, with the cumulative maximum subsidence reaching up to 98 mm and 83mm, while, for a cold season (13 October 2015 to 29 March 2016 of Stage A and 19 October 2016 to 12 March 2017 of Stage B), a relatively slow developing trend dominated those points, with a maximum subsidence of 31 mm and 45 mm, respectively, for the two periods. The potential reasons are suggested to be related to the air temperature, which influences the dissolution rate of mirabilite. The higher temperature of warm periods can accelerate the dissolution, and, accordingly, increased the subsiding velocities. Comparatively, lower temperature in cold periods slowed down the dissolution processing, which induced a stable trend of deformation. It should be noted that the dissolution rate of mirabilite in water is directly affected by solvent temperature (as shown in Table 7); however, it is indirectly affected by the air temperature. Hot water is used as solvent in drilling soluble production, which is delivered from the processing plant to the injection well after being measured and distributed at the control station. In the process of transportation, the solvent temperature is easily affected by the outside air temperature, which supports the above temperature-related interpretations.

Table 7. Seven groups of obtained InSAR-CTPIM parameters [28,40].

Mineral	Temperature (°C)										
	0	10	20	30	40	50	60	70	80	90	100
Thenardite	–	–	–	50.4	48.8	46.7	45.3	44.1	43.7	42.9	42.5
Glauber's Salt	5.0	9.0	19.4	40.8	–	–	–	–	–	–	–
Glauberite	0.18	0.19	0.20	0.21	0.21	–	0.21	0.20	0.20	–	0.16

It can also be determined, in Figure 20, that four minor jumps occurred for all the five feature points (marked by black arrows). According to the precipitation and temperature information of the Hunan Lixian Meteorological Bureau, the precipitation increased significantly on 13 October 2015, 16 May 2016, 31 October 2016, and 28 Jun 2017, as shown in Figure 21 [41]. Besides the decrease of solvent solubility caused by the aforementioned low temperature in winter, an increase of rainfall also contributed to the recoveries of subsidence.
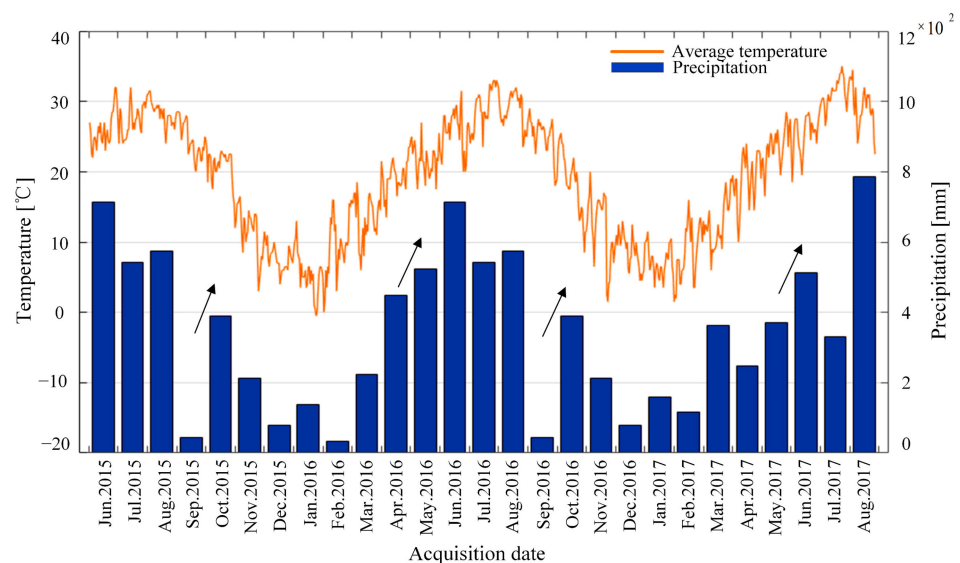

Figure 21. Air temperature and precipitation of the mining area (6 June 2016 to 31 January 2017) [42].

5. Conclusions

A novel InSAR deformation model, namely CT-PIM function, was proposed and applied for predicting the dynamic deformation over a drilling solution rock salt mine. The CT-PIM function was used as a substitute for traditional InSAR pure empirical models, which can also provide as potential combined use with other high-productive inspection methodologies, which has the following advantages: (1) with consideration of the physical underground mechanism, CT-PIM can describe the temporal dynamical characteristics of the mining-induced subsidence more realistically; (2) CT-PIM can be directly applied for the forward deformation prediction, which implements to the deficiency of non-consistency and unreasonableness between the traditional InSAR model (i.e., linear model or linear model combined with periodical function) and the forward prediction model (i.e., PIM); (3) it provides an alternative PIM parameters estimation method directly based on the InSAR phase observations, which can avoid the secondary error propagation from the InSAR inaccurate deformation to the subsequent deformation prediction; and, (4) as for the computational burden, since the GASM are based on the input InSAR unwrapped phases (not the final generated deformation sequences), we saved the preprocessing time for InSAR Geocoding compared to the static PIM.

The feasibility and improvement of our method was verified by both simulated and real-data experiments. The simulated results showed that the RMSE between the deformation results estimated by the new model and the simulated true value was ±4.5 mm, even under a high noise level of 0.65 rad. In the real data experiment, 32 Sentinel-1A SAR images were used to carry out the experiment over a water-soluble rock salt mine. As we determined, the maximum settlement was estimated as 294 mm. The experimental results were compared with external leveling results, and the RMSE was determined as ±10.9 mm, which accounts for only 6.9% of the maximum settlement. During the deformation prediction procedures, CT-PIM showed a considerable improvement of 32.7% than the traditional static PIM prediction approach, with an STD of ±12.9 mm compared to SBAS-generated results.

6. Patents

There are patents resulting from the work reported in this manuscript. Our research content has applied for a Chinese patent (ZL202010122691.8) entitled "A deformation monitoring method in mining area".

References

1. Ministry of Natural Resources. *China Mineral Resources Report*; Geological Publishing House: Beijing, China, 2019; pp. 2–6.
2. Zhang, M.G.; Wang, Z.S.; Wang, L.J.; Chen, Y.L.; Wu, Y.; Ma, D.; Zhang, K. Mechanism of collapse sinkholes induced by solution mining of salt formations and measures for prediction and prevention. *Bull. Eng. Geol. Environ.* **2019**, *78*, 1401–1415. [CrossRef]
3. Buchignani, V.; Avanzi, G.D.; Giannecchini, R.; Puccinelli, A. Evaporite karst and sinkholes: A synthesis on the case of Camaiore (Italy). *Environ. Geol.* **2008**, *53*, 1037–1044. [CrossRef]
4. Solari, L.; Montalti, R.; Barra, A.; Monserrat, O.; Crosetto, M. Multi-temporal satellite interferometry for fast-motion detection: An application to salt solution mining. *Remote Sens.* **2020**, *12*, 3919. [CrossRef]
5. Wang, S.; Jiang, G.; Weingarten, M.; Niu, Y. InSAR evidence indicates a link between fluid injection for salt mining and the 2019 Changning (China) earthquake sequence. *Geophys. Res. Lett.* **2020**, *47*, e2020GL087603. [CrossRef]
6. Furst, S.L.; Doucet, S.; Vernant, P.; Champollion, C.; Carme, J.L. Monitoring surface deformation of deep salt mining in vauvert (france), combining InSAR and leveling data for multi-source inversion. *Solid Earth* **2021**, *12*, 15–34. [CrossRef]
7. Jung, J.; Kim, D.J.; Vadivel, P.S.K.; Yun, S.H. Long-term deflection monitoring for bridges using X and C-Band time-series SAR interferometry. *Remote Sens.* **2019**, *11*, 1258. [CrossRef]
8. Tosti, F.; Gagliardi, V.; D'Amico, F.; Alani, A.M. Transport infrastructure monitoring by data fusion of GPR and SAR imagery information. *Transp. Res. Procedia* **2020**, *45*, 771–778. [CrossRef]
9. Gagliardi, V.; Bianchini Ciampoli, L.; Trevisani, S.; D'Amico, F.; Alani, A.M.; Benedetto, A.; Tosti, F. Testing Sentinel-1 SAR interferometry data for Airport Runway monitoring: A Geostatistical Analysis. *Sensors* **2021**, *21*, 5769. [CrossRef]
10. Zheng, M.; Deng, K.; Fan, H.; Du, S. Monitoring and analysis of surface deformation in mining area based on InSAR and GRACE. *Remote Sens.* **2018**, *10*, 1392. [CrossRef]
11. Xiao, L.; He, Y.G.; Xing, X.M.; Wen, D.B.; Tong, C.G.; Chen, L.F.; Yu, X.Y. Time series subsidence analysis of drilling solution mining rock salt mines based on Sentinel-1 data and SBAS-InSAR technique. *Int. J. Remote Sens.* **2019**, *23*, 501–513.
12. Ma, T.; Zhao, Y.J.; Zhang, W. Application of SBAS-InSAR technology in settlement monitoring of mining area. *Geom. Spat. Inf. Tech.* **2020**, *11*, 210–212.
13. Chen, Y.; Tong, Y.X.; Tan, K. Coal mining deformation monitoring using SBAS-InSAR and offset tracking: A case study of Yu County, China. *IEEE J. Sel. Top. Appl. Earth Obs. Remote Sens.* **2020**, *13*, 6077–6087. [CrossRef]
14. Yang, Z.F.; Li, Z.W.; Zhu, J.J.; Hu, J.; Wang, Y.J.; Chen, G.L. InSAR-Based model parameter estimation of probability integral method and its application for predicting mining-induced horizontal and vertical displacements. *IEEE Trans. Geosci. Remote Sens.* **2016**, *54*, 4818–4832. [CrossRef]
15. Fan, H.; Lu, L.; Yao, Y. Method combining probability integration model and a small baseline subset for time series monitoring of mining subsidence. *Remote Sens.* **2018**, *10*, 1444. [CrossRef]
16. Zhu, J.J. A Mining Monitoring Method Based on InSAR Technology. Chinese Patent ZL201310011306.2, 8 May 2013.
17. Li, Z.W.; Yang, Z.F.; Zhu, J.J.; Hu, J.; Wang, Y.J.; Li, P.X.; Chen, G.L. Retrieving three-dimensional displacement fields of mining areas from a single InSAR pair. *J. Geod.* **2015**, *89*, 17–32. [CrossRef]
18. Yang, Z.F.; Li, Z.W.; Zhu, J.J.; Preusse, A.; Yi, H.W.; Wang, Y.J.; Papst, M. An extension of the InSAR-Based probability integral method and its Application for Predicting 3-D Mining-Induced Displacements Under Different Extraction Conditions. *IEEE Trans. Geosci. Remote Sens.* **2017**, *55*, 3835–3845. [CrossRef]
19. Yang, Z.F.; Li, Z.W.; Zhu, J.J.; Feng, G.C.; Wang, Q.J.; Hu, J.; Wang, C.C. Deriving time-series three-dimensional displacements of mining areas from a single-geometry InSAR dataset. *J. Geod.* **2018**, *92*, 529–544. [CrossRef]
20. Xing, X.M.; Zhu, Y.K.; Yuan, Z.H.; Xiao, L.; Liu, X.B.; Chen, L.F.; Xia, Q.; Liu, B. Predicting mining-induced dynamic deformations for drilling solution rock salt mine based on probability integral method and weibull temporal function. *Int. J. Remote Sens.* **2020**, *42*, 639–671. [CrossRef]
21. Wang, L.Y.; Deng, K.Z.; Zheng, M.N. Research on ground deformation monitoring method in mining areas using the probability integral model fusion D-InSAR, sub-band InSAR and offset-tracking. *Int. J. Appl. Earth Obs.* **2020**, *85*, 101981. [CrossRef]
22. Xing, X.M.; Xiao, L.; Bao, L.; Chen, L.F.; Yuan, Z.H. An InSAR Prediction Method for Mining Subsidence in Drilling Water-Soluble Salt Mines. Chinese Patent ZL201910168502.8, 16 March 2021.
23. Zhu, G.Y.; Shen, H.X.; Wang, L.G. Study of dynamic prediction function of surface movement and deformation. *Chin. J. Rock Mech. Eng.* **2011**, *30*, 1889–1895.
24. Berardino, P.; Fornaro, G.; Lanari, R.; Sansosti, E. A new algorithm for surface deformation monitoring based on small baseline differential SAR interferograms. *IEEE Trans. Geosci. Remote Sens.* **2002**, *40*, 2375–2383. [CrossRef]
25. Lauknes, T.R.; Zebker, H.A.; Larsen, Y. InSAR Deformation Time Series Using an L1-Norm Small-Baseline Approach. *IEEE Trans. Geosci. Remote Sens.* **2010**, *49*, 536–546. [CrossRef]
26. Li, D.; Deng, K.Z.; Gao, X.X.; Niu, H.P. Monitoring and analysis of surface subsidence in mining areas based on SBAS-InSAR. *Geom. Inf. Sci. Wuhan Univ.* **2018**, *43*, 1531–1537.
27. Zhang, Y.; Meng, X.M.; Jordan, C.; Novellino, A.; Dijkstra, T.; Chen, G. Investigating slow-moving landslides in the Zhouqu region of China using InSAR time series. *Landslides* **2018**, *5*, 1299–1315. [CrossRef]
28. Wang, Q.M. *Water-Soluble Salt Mine Mining and Design*; Chemical Industry Press: Beijing, China, 2016; pp. 46–71.
29. Yao, L.; Sethares, W.A. Nonlinear parameter estimation via the genetic algorithm. *IEEE Trans. Signal Process.* **1994**, *42*, 927–935.

30. Xing, X.M.; Chang, H.C.; Chen, L.F.; Zhang, J.H.; Yuan, Z.H.; Shi, Z.N. Radar Interferometry Time Series to Investigate Deformation of Soft Clay Subgrade Settlement—A Case Study of Lungui Highway, China. *Remote Sens.* **2019**, *11*, 429. [CrossRef]
31. Tian, Y.G. *Study on Genetic Algorithm for Nonlinear Least Squares Estimation*; Wuhan University Press: Wuhan, China, 2003.
32. Xiao, H.F.; Tan, G.Z. Study on Fusing Simplex Search into Genetic Algorithm. *Comput. Eng. Appl.* **2008**, *44*, 30–33.
33. Yang, Z.F.; Li, Z.W.; Zhu, J.J.; Yi, H.W.; Feng, G.C. Deriving Dynamic Subsidence of Coal Mining Areas Using InSAR and Logistic Model. *Remote Sens.* **2017**, *9*, 125. [CrossRef]
34. Duan, M.; Xu, B.; Li, Z.W.; Wu, W.H.; Liu, J.H. Adaptively selecting interferograms for SBAS-InSAR based on graph theory and turbulence atmosphere. *IEEE Access* **2020**, *99*, 112898–112909. [CrossRef]
35. Goldstein, R.M.; Werner, C.L. Radar interferogram filtering for geophysical applications. *Geophys. Res. Lett.* **1998**, *25*, 4035–4038. [CrossRef]
36. Costantini, M.; Rosen, P.A. A generalized phase unwrapping approach for sparse data. In Proceedings of the IEEE International Geoscience and Remote Sensing Symposium, Hamburg, Germany, 28 June–2 July 1999; pp. 267–269.
37. Li, Z.W.; Ding, X.L.; Zheng, D.W.; Huang, C. Least squares-based filter for remote sensing image noise reduction. *IEEE Trans. Geosci. Remote Sens.* **2008**, *46*, 2044–2049. [CrossRef]
38. Fan, H.D.; Cheng, D.; Deng, K.Z.; Chen, B.Q.; Zhu, C.G. Subsidence monitoring using D-InSAR and probability integral prediction modelling in deep mining areas. *Surv. Rev.* **2015**, *47*, 438–445. [CrossRef]
39. Cannavo, F. Sensitivity analysis for volcanic source modeling quality assessment and model selection. *Comput. Geosci.* **2012**, *44*, 52–59. [CrossRef]
40. Ma, Z.Y.; Nie, C.X.; Wang, R.T. *Geological Basis and Mining Technology of Well and Mineral Salt*; National Mine Salt Industry Science and Technology Information Station: Chengdu, China, 1992; pp. 82–115.
41. Fomelis, M.; Papageorgiou, E.; Stamatopoulos, C. Episodic ground deformation signals in Thessaly Plain (Greece) revealed by data mining of SAR interferometry time series. *Int. J. Remote Sens.* **2016**, *37*, 3696–3711. [CrossRef]
42. Precipitation and Temperature Data of Lixian City, China. Available online: https://tianqi.911cha.com/lixian/2016.html (accessed on 15 December 2021).